Wet-spinning of ionic liquid@elastomer coaxial fibers with high stretchability and wide temperature resistance for strain sensors

Yang Xu [a], Qichun Feng [a], Chao Zhang [a,*], Tianxi Liu [a,b]

[a] *State Key Laboratory for Modification of Chemical Fibers and Polymer Materials, The Key Laboratory of High-Performance Fiber and Product, Ministry of Education, College of Materials Science and Engineering, Innovation Center for Textile Science and Technology, Donghua University, Shanghai, 201620, China*
[b] *Key Laboratory of Synthetic and Biological Colloids, Ministry of Education, School of Chemical and Material Engineering, Jiangnan University, Wuxi, 214122, China*

ABSTRACT

Integration of high wearing comfort, excellent conductivity and superior stretchability is required for wearable strain sensors. The construction of ionic conductors into elastic fibers and woven cloths can simultaneously realize wearing comfort and high elasticity. However, the fabrication of ionic conductive fibers with mechanical elasticity and high conductivity for fibrous strain sensors is challenging. Herein, a wet-spun encapsulation strategy is proposed for preparing a highly stretchable and fatigue-resistant ionic conductive fiber with a unique coaxial structure of ionic liquid core and thermoplastic elastomer sheath (IL@TPE). Particularly, the IL@TPE fiber exhibited a high stretchability of >250% and excellent ionic conductivity under a wide temperature range of −50 to 50 °C and long-term storage of >6 months. The as-assembled IL@TPE fibrous strain sensor exhibited excellent stability of >3000 cycles, low hysteresis, fast response time and high linearity for detecting human motions. The wet-spun encapsulation strategy for the fabrication of coaxial ionic fibers holds great promises for applications in smart wearable sensors with large stretchability, wide temperature resistance and high linearity.

1. Introduction

Ionic skin sensors are emerging pressure sensors that are capable of perceiving external stimuli of pressure, strain and torsion into electrical signals, showing wide application prospects in health monitoring, human-machine interfaces and soft robotics [1]. Ionic skin sensors can be directly worn or attached to human skin, effectively expanding the ability of human beings to perceive the external environment [2–12]. However, as a central component of ionic skin sensors, ionic conductors usually appear in forms of film or bulk, which are difficult to demonstrate high adaptability to curved surfaces of human skin as well as obtaining comfortable air permeability in practical applications [13]. Ionic conductors are highly expected to have characteristics of light-weight, mechanical flexibility and wide adaptability, to meet the requirements of high comfort and withstand high-frequency deformations that might occur under long-term conditions [14–16]. Weavings of conductive fibers into weft-knitted fabrics are capable of being adapted to complex motions of bending, torsion and stretching when worn on curved surfaces of human body [17–23]. More importantly, ionic conductive fibers give rise to ionic skin sensors with high permeability, wearable comfort, wear resistance and other characteristics difficult to

be realized by bulk sensor devices. However, the development of ionic conductive fibers with excellent mechanical flexibility, excellent fatigue resistance, high wearing comfort and wide temperature resistance is challenging.

Ionic liquids (IL) have been widely used in fields of catalytic synthesis, coordination chemistry, analytical chemistry and electrochemistry due to the integration of low vapor pressure, high ionic conductivity, excellent thermal stability and non-flammability [24]. These desirable properties and enormous structural diversities fuel the demands of IL as an ionic conductor in diverse applications [25]. Recently, IL was infused into elastic hollow fibers, which provided new ideas for the realization of elastic fibers [26]. However, the direct compounding of IL with fibrous materials faces problems of poor mechanical elasticity, easy absorption of water, and hard large-scale preparation, which greatly limit the development of IL-based fibrous materials for ionic skin sensors. More importantly, human skins are tissues that are directly exposed to toxic substances in working environments, and unfortunately to our best knowledge, the toxicity of IL on the skin has not been fully established [27]. Therefore, the development of IL-based ionic fibers adaptable to human skins has important prospects while meeting great challenges.

Herein, we present a wet-spun encapsulation strategy for the fabrication of a highly stretchable and fatigue-resistant ionic conductive fiber with a coaxial structure of IL core and thermoplastic elastomer sheath (IL@TPE). Among the coaxial structure of IL@TPE fiber, the IL core with good fluidity maintained an excellent ionic conductivity under large deformations and a wide temperature range of −50–50 °C, while the TPE sheath demonstrated excellent mechanical elasticity and ensured high environmental stability of encapsulated IL core. The resultant IL@TPE fibrous strain sensor exhibited a wide detecting range of 0–250%, high linear sensitivity (gauge factor: ~0.75), and long-term stability of 3000 cycles with low relaxation. The as-obtained IL@TPE fibrous strain sensors can be directly attached to human skins to monitor complex motions in real-time. The presented wet-spun encapsulation approach opens an avenue to fabricate highly stretchable and fatigue-resistant ionic conductive fibers for ionic and fibrous strain sensors with large sensitivity, wide operating temperature and high safety.

2. Materials and methods

2.1. Chemicals and reagents

1-Butyl-3-methylimidazolium tetrafluoroborate (IL) was purchased from Adamas. Styrene-isoprene-styrene block copolymer (TPE), ethanol, and dichloromethane (CH_2Cl_2) were purchased from Sigma-Aldrich. All the chemicals were used as received unless otherwise stated.

2.2. Preparation of IL@TPE fibers

Typically, 10 g of TPE and 20 g of CH2Cl2 were added into a flask and stirred at 100 rpm for 12 h, producing a spinning solution before degassing for 10 min. Wet-spun encapsulation fabrication of IL@TPE fiber was as follows: First, an inner-channel needle (21G) was inserted into an outer-channel needle (15G), and these two needles were fastened by sealing with a rubber [28]. Two syringe pumps were used to control the extrusion rates of inner (200 µL min^{-1}) and outer (400 µL min^{-1}) channels, respectively. The IL and sheath spinning solution were transferred to relevant syringes and extruded into a coagulation bath of ethanol. The production of IL@TPE fiber was fast and efficient, with the potential of continuously generated. Finally, the IL@TPE fiber was collected by a winding shaft and dried at 40 °C for 24 h. Similarly, coaxial needles with 19G@23G and 13G@17G structures were fabricated by changing the diameters of inner and outer channel needles. Neat TPE hollow fiber (h-TPE) was fabricated by washing away the IL core with ethanol and dried in an oven at 40 °C for 24 h [29].

2.3. Characterizations

Morphologies of fiber samples were measured by field-emission scanning electron microscopy (SEM, JSM-IT300). Mechanical tests were performed on a universal testing machine (SANS UTM2102) equipped with a 100 N sensor. Thermographic images were taken by an infrared thermal camera (TiS40, Fluke).

2.4. Measurements of strain sensors

The chain motions of isoprene and styrene segments endow the TPE sheath with two different glassy transition temperatures (−60, 70 °C). When the temperature exceeds 70 °C, the TPE sheath would melt from the solid state to form a viscous flowing state. In this study, a hot-pressing method was used to seal the two ends of IL@TPE fibers to prevent the leakage of the IL core. Both ends of the IL@TPE fibers were inserted with silver wires and quickly knotted to prevent the IL from out of hollow fibers. The hot-pressing conditions were set at 100 °C and 1 MPa for 30 s [30]. Both ends of IL@TPE fibers were completely sealed (Fig. S1). The as-obtained fibrous strain sensor was placed in a motorized actuating system, consisting of a tensile testing machine

(UTM2000, SANS) and a source meter (2612B, Keithley) [31].

3. Results and discussion

The fabrication procedure of IL@TPE fibers is shown in Fig. 1a. The CH_2Cl_2 solvent in the TPE/CH_2Cl_2 spinning solution was extracted by a coagulation bath, while the IL remained in the core. The wet-spun encapsulation strategy for the fabrication of IL@TPE fibers was efficient and easy for continuous preparation (Movie S1). Fig. S2 presented that the as-spun IL@TPE fibers were soaked in the coagulation bath. The IL@TPE fibers were collected by a winding shaft, and the continuous length of the fiber was more than 5 m (Fig. 1b), showing the potentials of large-scale production. Moreover, the IL@TPE fibers exhibited superior stretchability (Fig. 1c) and excellent mechanical properties (Fig. 1d). A cross-sectional optical image of the IL@TPE fiber is shown in Fig. 1e. The outer and inner diameters were estimated as 1000 and 900 µm, respectively. The surface of the IL@TPE fiber was smooth (Fig. 1f), and obvious hollow structures were observed (Fig. S3). The highly flexible and stretchable IL@TPE fibers were easily tied into knots (Fig. S4) and woven into fabrics (Fig. 1g).

Supplementary data related to this article can be found at https://doi.org/10.1016/j.coco.2021.100693.

Fig. 2a and b shows the typical stress-strain curves of IL@TPE and neat h-TPE fibers, respectively, at a tensile rate of 5 cm min^{-1}. The first cycle (0–100% strain) of the two curves showed a residual strain of 3–8%, attributed to the release of internal stress. After 100 cycles, the sheath TPE had an inevitable stress decrease reaching ~16% (Fig. 2a). The stress only decreased by ~28% after 5000 cycles, attributed to its stable coaxial structure [32–34]. To clearly show the differences in the stress decrease between the IL@TPE and h-TPE fibers, the maximum stresses of both the two fibers were normalized and showed in Fig. 2c. Compared to the IL@TPE fiber, the h-TPE fiber experienced a sharp stress decrease after 5000 cycles, which was much higher than that of IL@TPE fiber. The results showed that the mechanical properties of the h-TPE were improved by the IL core. The IL core played a lubricating role during the stretching process, which avoided the stress concentration [6,35–37]. Fig. S5a shows the optical photograph of the TPE pellets soaked in IL. The weight of TPE remained almost unchanged after being soaked in IL for more than 6 months, indicating that the TPE was highly stable in the IL (Fig. S5b). Fig. 2d exhibits the loading/unloading curves of IL@TPE fibers at different frequencies, and the symmetrical shapes of each time-stress curve showed that the IL@TPE fiber had a high elasticity [38].

Fig. 2e showed the stretching work (*U*) of the IL@TPE fiber was 0.076 mJ in the first cycle. The work remained at 0.076 mJ (Fig. 2f) when the unloading was complete, which was the value of energy dissipation (*ΔU*). The energy loss coefficient (η) was calculated from Equation (1):

$$\eta = \frac{\Delta U}{U} \tag{1}$$

The energy loss coefficient was calculated to be 0.18, and the energy dissipation was attributed to the plastic deformation of TPE.

Fig. 2g shows the mechanical properties of the IL@TPE fibers with different inner-channel diameters. With an increase of the inner-channel diameters, the thickness of the sheath decreased. However, the elongation at breaks of IL@TPE fibers increased slightly, and the fracture strength decreased gradually. The results were ascribed that the total mass of the sheath remained unchanged during tailoring the inner-channel diameters. Therefore, increasing the diameter of the inner channel would cause the sheath to become thin and with additional defects (Fig. S6) [39]. Similarly, adjusting the outer-channel diameter could also control the mechanical properties of the IL@TPE fibers (Fig. 2h). With an increase of the inner-channel diameter, the elongation at break and fracture strength of the IL@TPE fiber both increased slightly. The results were ascribed that the contents of IL in the IL@TPE
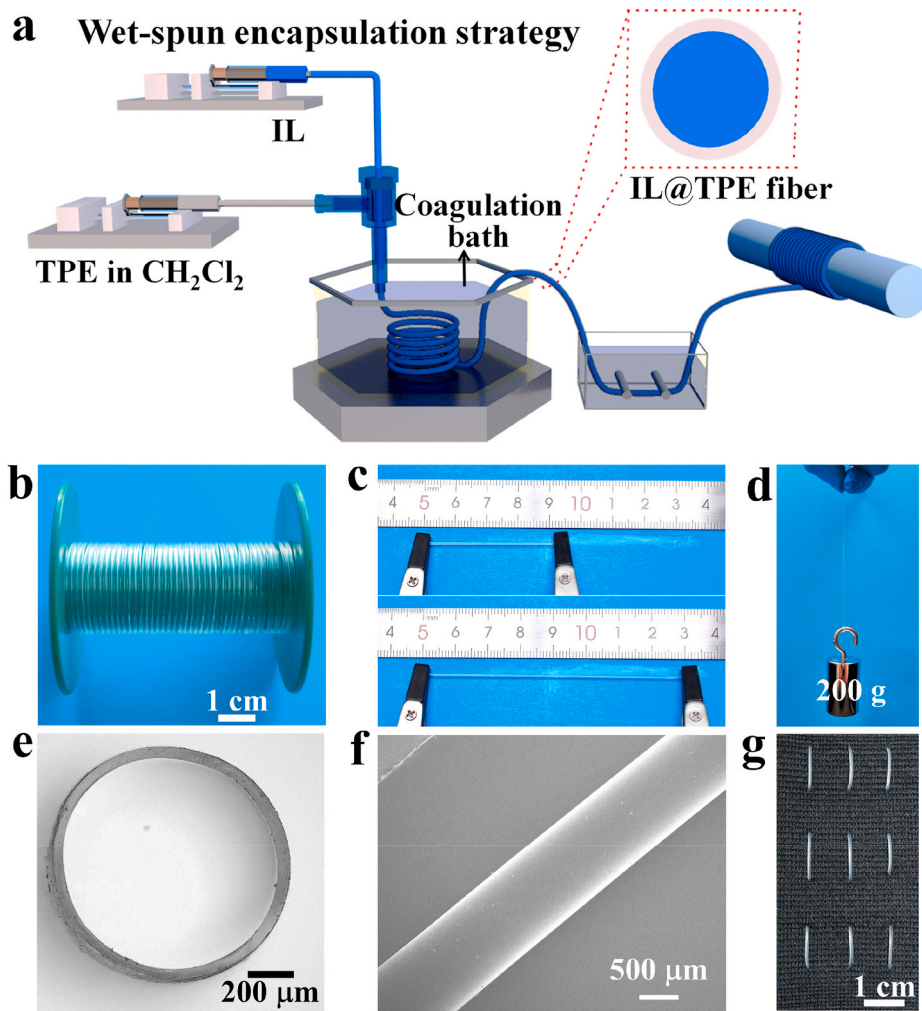
Fig. 1. Wet-spun encapsulation procedures and properties of IL@TPE fibers. (a) Schematic illustration of the wet-spun encapsulation strategy for fabricating IL@TPE fibers. (b) Photograph showing the IL@TPE fiber collected on a winding shaft. (c) Photographs showing the IL@TPE fiber stretched at a 100% strain. (d) Photograph showing the IL@TPE fiber holding a weight of 200 g. (e) Cross-section optical image of IL@TPE fiber. (f) Surface SEM image of IL@TPE fiber. (g) Photograph showing the IL@TPE fibers woven into a fabric.

fibers with different outer diameters were similar to each other. When the CH_2Cl_2 in TPE/CH_2Cl_2 spinning solution was extracted by the ethanol bath, all the sheath solution was contracted into the hollow fiber with a similar diameter (Fig. S7).

Temperature also significantly affected the mechanical properties of IL@TPE fibers (Fig. 2i). The elongations at break of IL@TPE fibers gradually increased with the rising temperatures (-50–50 °C), but the fracture strength gradually decreased. At low temperatures, the movement of TPE chains became restricted and the free volume between the chains decreased. When the TPE sheath was stretched under the maximum stress, the difficulty of molecular chain slip increased, and thus the elongation at break and fracture strength both decreased [40].

Fig. 3a showed the mechanism of the fibrous strain sensor. Young's modulus of IL was close to zero, and the volume of IL could not be compressed. During the tensile process, the shape of the IL core changed uniformly with the deformation of the sheath. The ideal volume change equation of IL during the deformation was:

$$d^2 L(1 + \Delta\varepsilon) = d_1^2 L \tag{2}$$

In Equation (2), $\Delta\varepsilon$ was the strain, d was the diameter of the outer channel, and L was the length of IL@TPE fiber. The actual Poisson's ratio of the sheath was less than 0.5, and its diameter changes were nonuniformity during the tensile. In the actual deformation, the IL deviated greatly from the ideal condition. The deviation was eliminated by introducing the deformation factor k, and the real volume change equation of IL during the deformation was:

$$kd^2 L(1 + \Delta\varepsilon) = d_1^2 L \tag{3}$$

where k was a parameter that was only related to TPE.

The initial resistance of IL@TPE fiber was R_0, and the equation for calculating the initial resistance was as follows:

$$R_0 = \rho \frac{L}{\pi(d_1/2)^2} = \rho \frac{4L}{\pi d_1^2} \tag{4}$$

where ρ was the conductivity of IL, and d_1 was the inner-channel diameter.

Combined with the three equations (2)–(4), the equation of real-time resistance of the IL@TPE fiber was as follows:

$$R = \rho \frac{4L(1 + \Delta\varepsilon)}{\pi d^2} \tag{5}$$

The calculation of gauge factors (GF) was as follows:

$$GF = \frac{\frac{R - R_0}{R_0}}{\Delta\varepsilon} \tag{6}$$

Therefore, the GF values of the IL@TPE fiber in its actual deformation was as follows:

$$GF = \frac{k(1 + \Delta\varepsilon)^2 - 1}{\Delta\varepsilon} \tag{7}$$

Mechanical properties of IL@TPE fibers were also characterized and showed in Fig. S8. The mechanical strength of the sensor was consistent
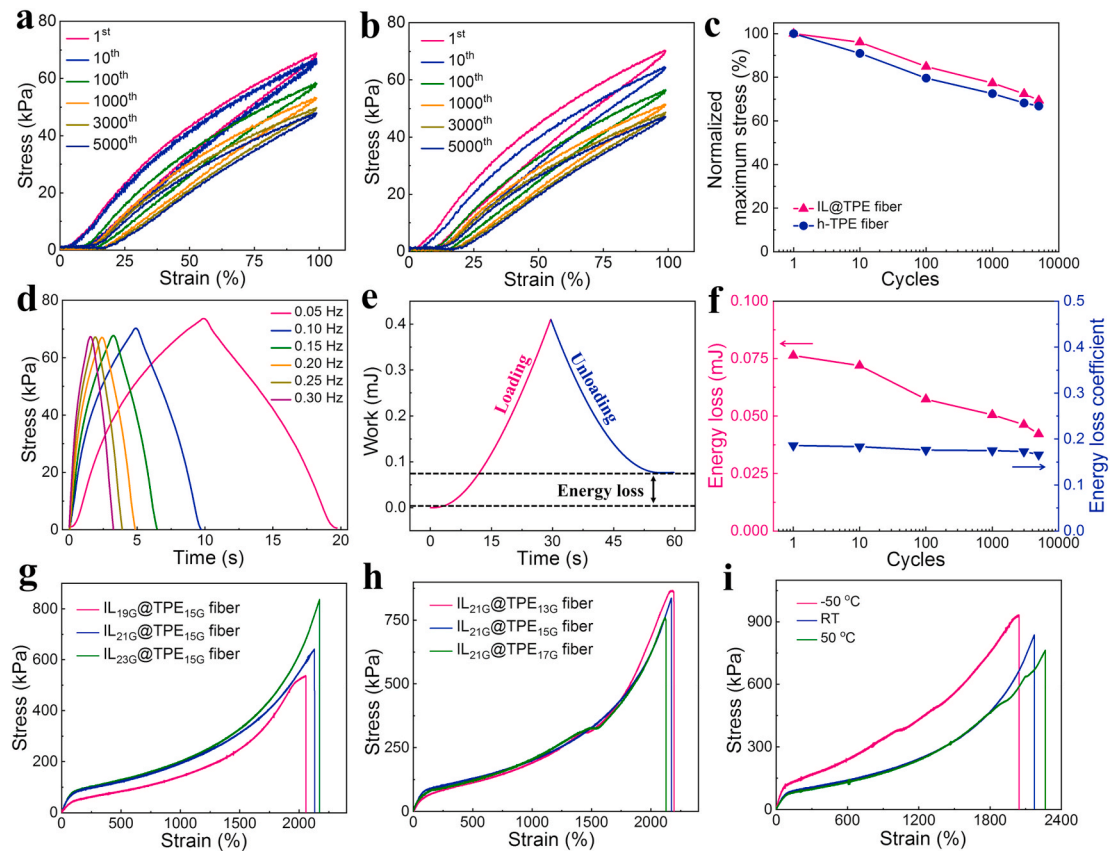
Fig. 2. Mechanical performance of IL@TPE fibers. Cyclic loading/unloading tests of (a) h-TPE and (b) IL@TPE fibers at a tensile rate of 5 cm min^{-1}. (c) Normalized maximum stress of h-TPE and IL@TPE fibers. (d) Time-dependent stress response of IL@TPE fiber at various loading/unloading rates (0–100% strain). (e) Tensile work and energy loss during the time-dependent loading/unloading stress response of IL@TPE fiber at the first cycle. (f) Cycle-dependent energy loss and energy loss coefficient of IL@TPE fiber. (g) Typical strain-stress curves of IL@TPE fibers with various inner-channel diameters. (h) Typical strain-stress curves of IL@TPE fibers with various out-channel diameters. (i) Typical strain-stress curves of IL@TPE fiber at various temperatures.

with the IL@TPE fiber due to the internal structure of the fiber was not damaged during the process of manufacturing the sensor. Fig. 3b is the hysteresis curve at a 100% strain, the curves of tensile and release were close to overlapping, and the enclosed area was very small, indicating that the hysteresis was slight. Fig. 3c showed that the response time of the strain sensor was 80 ms, attributed to the few micro defects in the IL@TPE fiber during wet-spinning. The resistance of the IL@TPE fiber remained stable after 10 min at a 100% strain, indicating the strain sensor had good conductivity and structural stability. Dynamic tensile loadings of different strains (0–250%) were applied to the IL@TPE fiber at a speed of 10 mm min^{-1}. Fig. S9a showed stable and repetitive signals under different strains, indicating that the sensor had high stability in a wide strain range. Fig. S9b shows cyclic tensile response curves of the sensor in the frequency range of 0.01–0.1 Hz. The working curves of the strain sensor matched the measured signals completely at different frequencies, indicating the strain sensor was able to adapt to a complex frequency environment [41]. To demonstrate the durability, the strain sensor was stretched for 18,000 s (>3000 cycles) under 100% strain (Fig. S9c). The insets of the enlarged area showed excellent repeatability during cycling, indicating the strain sensor was stable to work for a long time. Fig. S10a is the time-weight experiments of the IL@TPE fibers at different temperatures. The weight of IL@TPE fiber remained ~98% after aging for 6 months at low, room and high temperatures, respectively, indicating the efficiency of the hot-pressing sealing and the hydrophobicity of the TPE sheath. Fig. S10b is the time-conductivity experiments of the IL@TPE fibers at different temperatures. The ionic conductivity of the IL@TPE fibers was as high as 0.45 S m^{-1} at room temperature and showed a positive correlation with the increase of temperatures. This was attributed to the ionic conductivity of IL was

highly related to the temperature. Fig. S10c shows the GF values of the sensor at different temperatures, and the GF values were calculated as 0.74 (R^2 = 0.99), 0.77 (R^2 = 0.99), 0.77 (R^2 = 0.99), 0.76 (R^2 = 0.99), and 0.75 (R^2 = 0.99) at −50, −25, 0, 25, and 50 °C, respectively. From Equation (7), although the temperature had a significant effect on the ionic conductivity of IL, the GF values showed no obvious changes because the GF values were related to the shape of the sheath. Fig. 3d and e are schematic illustrations of the stretching of fabrics woven by IL@TPE fibers at high and low temperatures, respectively. The fabrics could be stretched at 50 °C and −30 °C, respectively. This was attributed to a wide liquid-state temperature range of the IL core, and the TPE had good mechanical elasticity at such temperatures.

Fig. 3f–h and S11 are the proof-of-concept sensing measurements of IL@TPE fibers as a wearable strain sensor. The illustrations were optical photographs of the IL@TPE fiber sensor stick to the skin of human joints of elbow, wrist, finger and knee. Fig. 3f showed that the strain sensor was integrated into the wrist skin, which accurately monitored the bending movement of the human wrist and got a series of accurate working curves. Fig. 3g showed that the IL@TPE fiber strain sensor could well monitor the elbow motion of bending and recovery. Besides, when the elbow bent to different angles, the changes of relative resistance signals were repeatable, and the bending angles of the finger could be accurately tracked by monitoring the changes of relative resistances (Fig. 3h). This was due to the strain sensor had stable GF values within a wide strain range and no interference from the core. Similarly, the IL@TPE fiber strain sensors were integrated onto the skin of the knee and finger, and the motions of these joints could also be monitored, resulting in the corresponding working curves (Figs. S11a and S11b). The working curves could accurately simulate the motion of finger joints
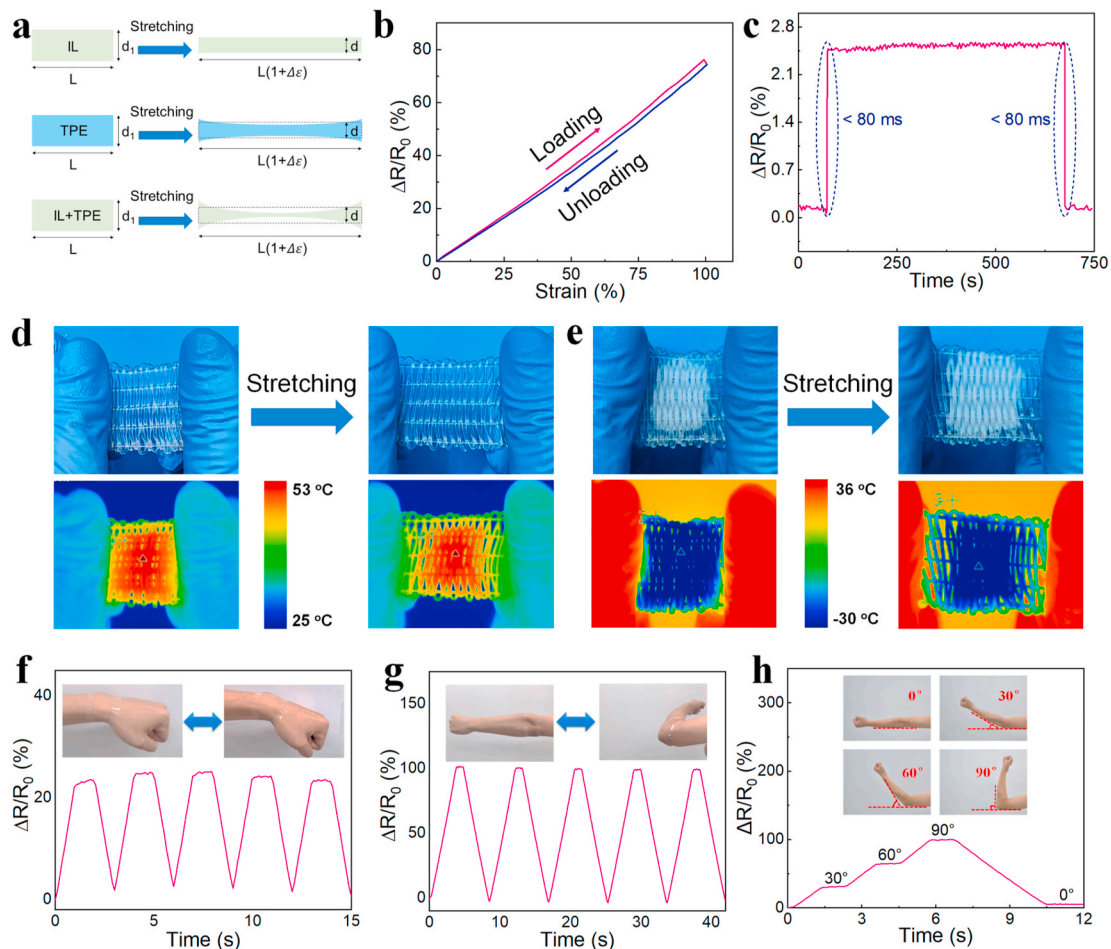
Fig. 3. Strain sensing performance of wearable strain sensors based on IL@TPE fibers. (a) Schematic of the reversible macroscopic shape change of fibrous strain sensors during stretching. (b) Hysteresis performance of IL@TPE fibrous strain sensor. (c) Response time of IL@TPE fibrous strain sensor. Photographs showing the stretching processes of IL@TPE-based woven fabrics at (d) high and (e) low temperatures. The IL@TPE fibrous strain sensor monitoring (f) wrist and (g) elbow bending of a volunteer. (h) IL@TPE fibrous strain sensor monitoring elbow motion of various bending angles.

at different angles (Fig. S11c). These results showed the IL@TPE fiber strain sensor had high sensitivity, wide strain range and good wearability.

4. Conclusion

In summary, a fibrous strain sensor with a core-sheath structure was fabricated by the wet-spun encapsulation strategy. The IL core endowed the IL@TPE fibers with high ionic conductivity reaching ~0.45 S m^{-1}. The hydrophobicity of the TPE sheath ensured the mass changes of the IL@TPE fibers less than 2% after being placed at low and high temperatures for at least 6 months (−50–50 °C). Both theoretical estimates and experimental results proved that the working curves of the IL@TPE fibrous strain sensor were related to the sheath structure, while not the environmental temperatures or ionic conductivities of the IL core. The IL@TPE fibrous strain sensor could work stably in a complex environment (0.01–0.1 Hz and 0%–250% strain). The IL@TPE fibrous strain sensor also manifested high cycling stability (>3000 cycles) by running stably for more than 18,000 s in the strain range of 0%–100%. Besides, the wearability of the IL@TPE fiber was conceptually verified. The IL@TPE fibrous strain sensor was integrated onto the human skin of the elbow, wrist and knee joints, which could monitor small and large deformation movements of human joints in real-time as well as accurately capturing the subtle changes of human joints at different angles. The wet-spun encapsulation strategy thus opens a new avenue to fabricate fibrous ionic conductors and strain sensors with high sensitivity, excellent wearing comfort, and tolerance to extreme temperatures.

CRediT authorship contribution statement

Yang Xu: Visualization, Investigation, Data curation, Writing – original draft. **Qichun Feng:** Visualization, Investigation, Data curation, Writing – review & editing. **Chao Zhang:** Conceptualization, Methodology, Supervision, Writing – review & editing, Supervision. **Tianxi Liu:** Conceptualization, Supervision.

Declaration of competing interest

The authors declare that they have no known competing financial interests or personal relationships that could have appeared to influence the work reported in this paper.

Acknowledgments

Appendix A. Supplementary data

Supplementary data to this article can be found online at https://doi.org/10.1016/j.coco.2021.100693.

References

[1] Z.W.K. Low, Z. Li, C. Owh, P.L. Chee, E. Ye, D. Kai, D.P. Yang, X.J. Loh, Using artificial skin devices as skin replacements: insights into superficial treatment, Small 15 (2019) 1805453.

[2] V. Amoli, J.S. Kim, E. Jee, Y.S. Chung, S.Y. Kim, J. Koo, H. Choi, Y. Kim, D.H. Kim, A bioinspired hydrogen bond-triggered ultrasensitive ionic mechanoreceptor skin, Nat. Commun. 10 (2019) 4019–4032.

[3] Z. Lei, Q. Wang, S. Sun, W. Zhu, P. Wu, A bioinspired mineral hydrogel as a self-healable, mechanically adaptable ionic skin for highly sensitive pressure sensing, Adv. Mater. 29 (2017) 1700321.

[4] Z. Lei, P. Wu, Zwitterionic skins with a wide scope of customizable functionalities, ACS Nano 12 (2018) 12860–12868.

[5] Z. Lei, W. Zhu, X. Zhang, X. Wang, P. Wu, Bio-inspired ionic skin for theranostics, Adv. Funct. Mater. 30 (2020) 2008020.

[6] M. Cai, Q. Yu, W. Liu, F. Zhou, Ionic liquid lubricants: when chemistry meets tribology, Chem. Soc. Rev. 49 (2020) 7753–7818.

[7] Z. Liu, Y. Wang, Y. Ren, G. Jin, C. Zhang, W. Chen, F. Yan, Poly(ionic liquid) hydrogel-based anti-freezing ionic skin for a soft robotic gripper, Mater. Horiz. 7 (2020) 919–927.

[8] K. Parida, V. Kumar, W. Jiangxin, V. Bhavanasi, R. Bendi, P.S. Lee, Highly transparent, stretchable, and self-healing ionic-skin triboelectric nanogenerators for energy harvesting and touch applications, Adv. Mater. 29 (2017) 1702181.

[9] Z. Qiu, Y. Wan, W. Zhou, J. Yang, J. Yang, J. Huang, J. Zhang, Q. Liu, S. Huang, N. Bai, Z. Wu, W. Hong, H. Wang, C.F. Guo, Ionic skin with biomimetic dielectric layer templated from calathea zebrine leaf, Adv. Funct. Mater. 28 (2018) 1802343.

[10] J.Y. Sun, C. Keplinger, G.M. Whitesides, Z. Suo, Ionic skin, Adv. Mater. 26 (2014) 7608–7614.

[11] X.Y. Yin, Y. Zhang, J. Xiao, C. Moorlag, J. Yang, Monolithic dual-material 3D printing of ionic skins with long-term performance stability, Adv. Funct. Mater. 29 (2019) 1904716.

[12] B. Ying, Q. Wu, J. Li, X. Liu, An ambient-stable and stretchable ionic skin with multimodal sensation, Mater. Horiz. 7 (2020) 477–488.

[13] V. Amoli, J.S. Kim, S.Y. Kim, J. Koo, Y.S. Chung, H. Choi, D.H. Kim, Ionic tactile sensors for emerging human-interactive technologies: a review of recent progress, Adv. Funct. Mater. 30 (2019) 1904532.

[14] H. Wang, Z. Wang, J. Yang, C. Xu, Q. Zhang, Z. Peng, Ionic gels and their applications in stretchable electronics, Macromol. Rapid Commun. 39 (2018) 1800246.

[15] J. Mao, C. Zhao, Y. Li, D. Xiang, Z. Wang, Highly stretchable, self-healing, and strain-sensitive based on double-crosslinked nanocomposite hydrogel, Compos. Commun. 17 (2020) 22–27.

[16] M. Tang, R. Zhang, J. Fang, S. Li, Y.-X. Xu, G. Huang, Ductile composites with strain hardening behavior constructing highly sensitive electronic sensor, Compos. Commun. 15 (2019) 20–24.

[17] M. Amjadi, K.-U. Kyung, I. Park, M. Sitti, Stretchable, skin-mountable, and wearable strain sensors and their potential applications: a review, Adv. Funct. Mater. 26 (2016) 1678–1698.

[18] Z. Liu, F. Mo, H. Li, M. Zhu, Z. Wang, G. Liang, C. Zhi, Advances in flexible and wearable energy-storage textiles, Small Methods 2 (2018) 1800124.

[19] W. Zeng, L. Shu, Q. Li, S. Chen, F. Wang, X.M. Tao, Fiber-based wearable electronics: a review of materials, fabrication, devices, and applications, Adv. Mater. 26 (2014) 5310–5336.

[20] Q. Gao, M. Wang, X. Kang, C. Zhu, M. Ge, Continuous wet-spinning of flexible and water-stable conductive PEDOT:PSS/PVA composite fibers for wearable sensors, Compos. Commun. 17 (2020) 134–140.

[21] W. Yuan, J. Yang, F. Yin, Y. Li, Y. Yuan, Flexible and stretchable MXene/Polyurethane fabrics with delicate wrinkle structure design for effective electromagnetic interference shielding at a dynamic stretching process, Compos. Commun. 19 (2020) 90–98.

[22] X. Yue, Y. Jia, X. Wang, K. Zhou, W. Zhai, G. Zheng, K. Dai, L. Mi, C. Liu, C. Shen, Highly stretchable and durable fiber-shaped strain sensor with porous core-sheath structure for human motion monitoring, Compos. Sci. Technol. 189 (2020) 108038.

[23] J. Zhou, G. Tian, G. Jin, Y. Xin, R. Tao, G. Lubineau, Buckled conductive polymer ribbons in elastomer channels as stretchable fiber conductor, Adv. Funct. Mater. 30 (2019) 1907316.

[24] L.C. Tome, I.M. Marrucho, Ionic liquid-based materials: a platform to design engineered CO2 separation membranes, Chem. Soc. Rev. 45 (2016) 2785–2824.

[25] O. Nordness, J.F. Brennecke, Ion dissociation in ionic liquids and ionic liquid solutions, Chem. Rev. 120 (2020) 12873–12902.

[26] S. Chen, H. Liu, S. Liu, P. Wang, S. Zeng, L. Sun, L. Liu, Transparent and waterproof ionic liquid-based fibers for highly durable multifunctional sensors and strain-insensitive stretchable conductors, ACS Appl. Mater. Interfaces 10 (2018) 4305–4314.

[27] K. Gao, B. Li, R. Chen, P. Qian, J. Dong, C. Xue, X. Guo, X. Deng, A feasibility study of using silkworm larvae as a novel in vivo model to evaluate the biotoxicity of ionic liquids, Ecotoxicol. Environ. Saf. 209 (2020) 111759–111769.

[28] J. Zhou, X. Xu, Y. Xin, G. Lubineau, Coaxial thermoplastic elastomer-wrapped carbon nanotube fibers for deformable and wearable strain sensors, Adv. Funct. Mater. 28 (2018) 1705591.

[29] H. Guo, Q. Feng, K. Xu, J. Xu, J. Zhu, C. Zhang, T. Liu, Self-templated conversion of metallogel into heterostructured tmp@carbon quasiaerogels boosting bifunctional electrocatalysis, Adv. Funct. Mater. 29 (2019) 1903660.

[30] K. Ruan, Y. Guo, Y. Tang, Y. Zhang, J. Zhang, M. He, J. Kong, J. Gu, Improved thermal conductivities in polystyrene nanocomposites by incorporating thermal reduced graphene oxide via electrospinning-hot press technique, Compos. Commun. 10 (2018) 68–72.

[31] Y. Wang, M. Tebyetekerwa, Y. Liu, M. Wang, J. Zhu, J. Xu, C. Zhang, T. Liu, Extremely stretchable and healable ionic conductive hydrogels fabricated by surface competitive coordination for human-motion detection, Chem. Eng. J. (2020) 127637–127647.

[32] L. Li, Y. Zhang, H. Lu, Y. Wang, J. Xu, J. Zhu, C. Zhang, T. Liu, Cryopolymerization enables anisotropic polyaniline hybrid hydrogels with superelasticity and highly deformation-tolerant electrochemical energy storage, Nat. Commun. 11 (2020) 62–74.

[33] M. Liu, P. Zhang, Z. Qu, Y. Yan, C. Lai, T. Liu, S. Zhang, Conductive carbon nanofiber interpenetrated graphene architecture for ultra-stable sodium ion battery, Nat. Commun. 10 (2019) 3917–3928.

[34] F. Zhang, Y. Feng, M. Qin, L. Gao, Z. Li, F. Zhao, Z. Zhang, F. Lv, W. Feng, Stress controllability in thermal and electrical conductivity of 3D elastic graphene-crosslinked carbon nanotube sponge/polyimide nanocomposite, Adv. Funct. Mater. 29 (2019) 1901383.

[35] K. Ruan, X. Shi, Y. Guo, J. Gu, Interfacial thermal resistance in thermally conductive polymer composites: a review, Compos. Commun. 22 (2020) 100518.

[36] P. Song, B. Liu, H. Qiu, X. Shi, D. Cao, J. Gu, MXenes for polymer matrix electromagnetic interference shielding composites: a review, Compos. Commun. 24 (2021) 100653.

[37] Y. Guo, K. Ruan, X. Shi, X. Yang, J. Gu, Factors affecting thermal conductivities of the polymers and polymer composites: a review, Compos. Sci. Technol. 193 (2020) 108134.

[38] M. Qin, Y. Xu, R. Cao, W. Feng, L. Chen, Efficiently controlling the 3D thermal conductivity of a polymer nanocomposite via a hyperelastic double-continuous network of graphene and sponge, Adv. Funct. Mater. 28 (2018) 1805053.

[39] I.H. Kim, T. Yun, J.E. Kim, H. Yu, S.P. Sasikala, K.E. Lee, S.H. Koo, H. Hwang, H. J. Jung, J.Y. Park, H.S. Jeong, S.O. Kim, Mussel-inspired defect engineering of graphene liquid crystalline fibers for synergistic enhancement of mechanical strength and electrical conductivity, Adv. Mater. 30 (2018) 1803267.

[40] J.C. Cui, Y. Li, D. Chen, T.G. Zhan, K.D. Zhang, Ionic liquid-based stimuli-responsive functional materials, Adv. Funct. Mater. 30 (2020) 2005522.

[41] Y. Zhao, M. Ren, Y. Shang, J. Li, S. Wang, W. Zhai, G. Zheng, K. Dai, C. Liu, C. Shen, Ultra-sensitive and durable strain sensor with sandwich structure and excellent anti-interference ability for wearable electronic skins, Compos. Sci. Technol. 200 (2020) 108448.